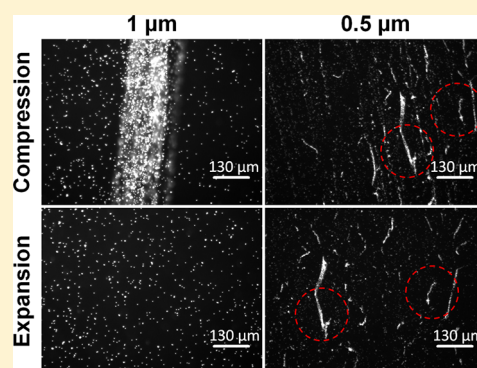


## Particle Size Effects on Collapse in Monolayers

Chin-Chang Kuo, Akihisa T. Kodama, Thomas Boatwright, and Michael Dennin\*

Department of Physics and Astronomy, University of California, Irvine, California 92697, United States

**ABSTRACT:** We report on the impact of differently sized particles on the collapse of a Langmuir monolayer. We use an SDS–DODAB monolayer because it is known to collapse reversibly under compression and expansion cycles. Particles with diameters of 1  $\mu\text{m}$ , 0.5  $\mu\text{m}$ , 0.1  $\mu\text{m}$ , and 20 nm are deposited on the SDS–DODAB monolayer. We find a critical particle size range of 0.1 to 0.5  $\mu\text{m}$  that produces a transition from reversible to irreversible collapse. The nature of the collapse is determined through optical observations and surface pressure measurements. In addition, although 20 nm particles do not cause irreversible collapse in the monolayer, they significantly decrease the collapse pressure relative to the other systems. Therefore, we observe three distinct collapse behaviors—reversible, irreversible, and reversible at a reduced surface pressure.



## ■ INTRODUCTION

The nature of collapse of thin sheets of material under compression has received recent theoretical and experimental attention.<sup>1–5</sup> Of particular interest is folding in Langmuir monolayers.<sup>6–11</sup> A Langmuir monolayer consists of a single layer of amphiphilic molecules confined to the interface between air and an aqueous subphase. By changing the interfacial area, Langmuir monolayers exhibit a range of interesting behaviors. Numerous phases occur, ranging from a gaslike phase to more condensed phases as the surface density increases.<sup>12</sup> Once the molecules become sufficiently packed, a transition from a 2D to 3D structure occurs, which is referred to as collapse. During this transition, the surface pressure remains approximately constant under further compression. There are several mechanisms of monolayer collapse, such as buckling, budding, and vesiculation.<sup>13–17</sup> A special and interesting type of collapse for monolayers is folding. It is characterized by the formation of a 3D structure that extends along a quasi-1D boundary and forms a bilayer that submerges into the subphase. Folds can extend perpendicular to the axis of compression<sup>10,11</sup> across the entire width of a Langmuir trough, usually on the order of centimeters, and submerge millimeters below the interface.

The collapse of a monolayer can be classified as either reversible or irreversible under cyclic compression and expansion. Reversible collapse maintains the monolayer from cycle to cycle, and in irreversible collapse, molecules are lost from the monolayer during each cycle. Most examples of reversible collapse are in systems that exhibit folding. An interesting example of reversible folding occurs in lung surfactant. Lung surfactant is a thin coating on the small air sacs deep in the lung, known as alveoli. Here, gases in the lung are exchanged with the blood.<sup>18</sup> The surfactant plays a significant role in respiration by lowering the surface tension to near zero values at the air–water interface, reducing the work required to inflate and deflate the lung. The lowering of

surface tension also regulates the air pressure in neighboring alveoli by greatly reducing the Laplace pressure (for a sphere,  $\Delta P = (2\gamma)/(r)$  where  $r$  is the radius and  $\gamma$  is the surface tension).<sup>19</sup> This prevents the flow of air from small alveoli to larger ones. To maintain a minimal surface tension throughout respiration, lung surfactant forms giant folds at high compression.<sup>7,9</sup> It is important that this process be reversible so that the lung does not have to regenerate the surfactant. Of interest to the public health is how pollutants and other airborne particulate matter affect the functionality of the lung surfactant. Inhaled particulate matter may interfere with the folding of the film and cause adverse health effects.<sup>20–22</sup> Understanding how particles of different sizes impact the folding dynamics on this scale is an important issue.<sup>23–26</sup>

In this article, we focus on the impact of particles of different sizes on the collapse of a monolayer. This can provide insight into mechanisms of particle–surfactant interaction in biological systems. We use a catanionic monolayer as a model. This is produced by mixing sodium dodecyl sulfate (SDS), which has a positive charge, and dioctadecyldimethylammonium bromide (DODAB), which has a negative charge,<sup>10,11,27</sup> in a 1:1 ratio to form a stable monolayer. Behavior consistent with giant reversible folds has been observed in this system.<sup>10</sup> Under expansion from a collapsed state, two distinct regimes have been observed using tracer particles embedded in the monolayer. There is an initial period during which collapsed regions remain unaffected and the surrounding monolayer stretches elastically. Once a critical stress is reached, the collapsed regions release material back into the monolayer as they “unfold”. During this unfolding phase, the surface pressure remains essentially constant.<sup>11</sup> Under the addition of particles, we observe two main changes to this collapse behavior: (a) the

Received: April 17, 2012

Revised: July 2, 2012

Published: August 24, 2012

elimination of the unfolding phase on expansion, resulting in irreversible collapse, and (b) a reduction of the collapse pressure. This results in three regimes: (a) reversible collapse, (b) irreversible collapse, and (c) reversible collapse at a reduced surface pressure.

The rest of the article is organized as follows. In the Materials and Methods section, we introduce experimental methods for preparing the SDS–DODAB monolayer and depositing particle solutions. We then show the optical observation and isotherm measurements for different particle sizes. Then we apply an analysis estimating the average effective molecular area, which allows us to quantify the amount of material lost and the change in folding pressure after each isotherm cycle. Finally, we propose a possible explanation (without chemical reactions) for our experimental results that is related to the ratio of particle size to the SDS–DODAB preferred collapse curvature.

## MATERIALS AND METHODS

We used a 1:1 mixture of DODAB (97% purity) and SDS (99% purity) to produce an SDS–DODAB monolayer. An SDS stock solution is prepared by dissolving SDS in ethanol to make a 1.2 mM solution. DODAB stock solution is prepared by dissolving DODAB in chloroform to make a 1.2 mM solution. Equimolar mixtures SDS–DODAB are prepared by mixing the same amount of the stock solutions and then diluting with chloroform to 0.12 mM.

We prepare all particle solutions with a consistent procedure. Carboxylate-modified microsphere solutions (Invitrogen, red fluorescence, 2% solids) with the following particle diameters are used: 1  $\mu\text{m}$ , 0.5  $\mu\text{m}$ , 0.1  $\mu\text{m}$ , and 20 nm. The concentrated particle solutions all have the same percentage of mass per volume, so solutions with different particle diameters have different numbers of particles per unit volume. It is worth noting that all sizes of particles have the same small concentrations of surfactants that are used to prevent particle aggregation. A 1:1 mixture of the concentrated particle solution and methanol are used to enhance the spreading on the surface. The particle concentrations in each solution are  $1.35 \times 10^{10}$ ,  $1.55 \times 10^{11}$ ,  $1.35 \times 10^{13}$ , and  $1.3 \times 10^{15}$  particles/mL for 1  $\mu\text{m}$ , 0.5  $\mu\text{m}$ , 0.1  $\mu\text{m}$ , and 20 nm solutions, respectively. For weakly fluorescent 20 nm particles, a small amount (1% of the SDS–DODAB molecular concentration) of fluorescent probe 2-(12-(7-nitrobenz-2-oxa-1,3-diazol-4-yl)amino)dodecanoyl-1-hexadecanoyl-*sn*-glycero-3-phosphocholine (NBD C12-HPC) is added to the SDS–DODAB solution. We only use the fluorescent probe to visualize the folding of the monolayer.

The schematic in Figure 1 illustrates the main experimental steps. The first step is the preparation of an SDS–DODAB monolayer on the water surface in a Langmuir trough (Nima model 102M). We

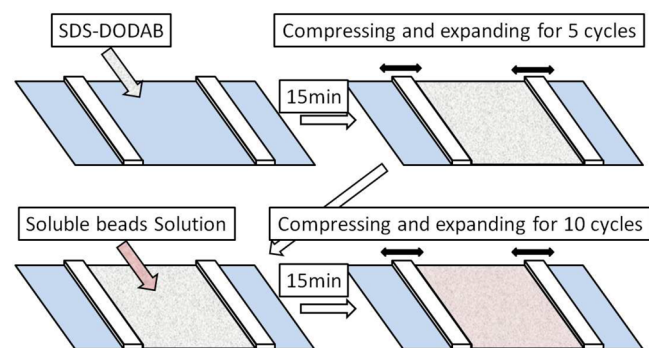


**Figure 1.** Schematic of the experiment. The SDS–DODAB solution and particle solution are deposited on the water surface from a syringe. We wait about 15 min before compression and expansion cycles for the solvent to evaporate. The particles are then added to the surface, followed by another 15 min waiting period.

placed 65 mL of ultrapure water (Millipore Milli-Q) in the well-cleaned Langmuir trough and then deposited 100  $\mu\text{L}$  of SDS–DODAB solution to form a monolayer. The deposition of the SDS–DODAB monolayer is accomplished by contacting a droplet of the solution from the tip of a syringe on the surface and allowing it to spread by surface tension. Evenly distributing the SDS–DODAB solution across the trough contributes to a more homogeneous monolayer. We waited 15 min to ensure that the chloroform and ethanol in the SDS–DODAB solution completely evaporate from the trough. Afterward, we began isotherm compression and expansion cycles and measuring five cycles to confirm the previously observed collapse behavior of the SDS–DODAB monolayer. Once this is established, various amounts of particle solution with different particle sizes were distributed evenly on the surface. The amounts of particle solutions range from 25 to 150  $\mu\text{L}$  in 25  $\mu\text{L}$  increments. The deposition of particle solutions follow the same method as used for the SDS–DODAB solution. We then waited another 15 min for the evaporation of methanol from the interface. Ten more compression and expansion cycles were used to study the effect of particles on the collapse of the monolayer.

It is worth noting that not all of the particles remain on the surface; a fraction of the particles dissolve into the subphase after the deposition. Therefore, it is difficult to estimate the surface concentration of particles deposited at the interface quantitatively. One option for characterizing the number of particles on the surface is to use the shifts in the isotherm after deposition. Unfortunately, this is complicated by a lack of knowledge regarding the precise location of the particles relative to the monolayer. We discuss this issue in more detail when we present the isotherm results. Because we do not have precise information on the number of particles in the system, we studied a range of deposition volumes in order to change the total number of particles in the monolayer. We will show that the results are relatively independent of the number of particles. Therefore, our inability to quantify the number of particles on the surface precisely does not have a significant impact on our results.

Isotherm measurements and observations using an optical microscope provide quantitative and qualitative information about the system. Isotherm measurements are controlled by Nima software, which records surface pressure from a tensiometer, from which hangs a Wilhelmy plate. The orientation of the Wilhelmy plate is perpendicular to the major axis of the barriers. There is no significant change in the plate orientation during the isotherm cycles. The surface area is changed from 80 to 19  $\text{cm}^2$  at a rate of 15  $\text{cm}^2$  per minute. The surface pressure is recorded for both pure SDS–DODAB monolayers and SDS–DODAB monolayers with particles. After the isotherm measurements of all cycles, we use an optical microscope (Olympus BX60MF5) with a charge-coupled-device camera (CCD) to observe and record the folding dynamics corresponding to the different particles sizes. A 10 $\times$  magnification objective is used to magnify the monolayer images. The reversible and irreversible collapse of the SDS–DODAB monolayer can be observed with this procedure.

## RESULTS

**Experimental Observation.** Compression and expansion images of SDS–DODAB monolayers with different sizes of particles embedded in them are shown in Figure 2. The images are taken after the fifth cycle of compression. For 1  $\mu\text{m}$  particles (Figure 2a,e), a region of collapse approximately 200  $\mu\text{m}$  wide is observed under compression. The bright spots are the fluorescence from 1  $\mu\text{m}$  particles. This result is similar to the observed giant folds in an SDS–DODAB monolayer.<sup>11</sup> The difference between these studies and the work in Boatwright et al.<sup>11</sup> is the number of particles deposited. The concentration here is about 100 times larger than the concentration used in previous work. Despite this difference, the single folding and unfolding dynamics for SDS–DODAB plus 1  $\mu\text{m}$  particles matches the previous work reported by Boatwright et al.<sup>11</sup>

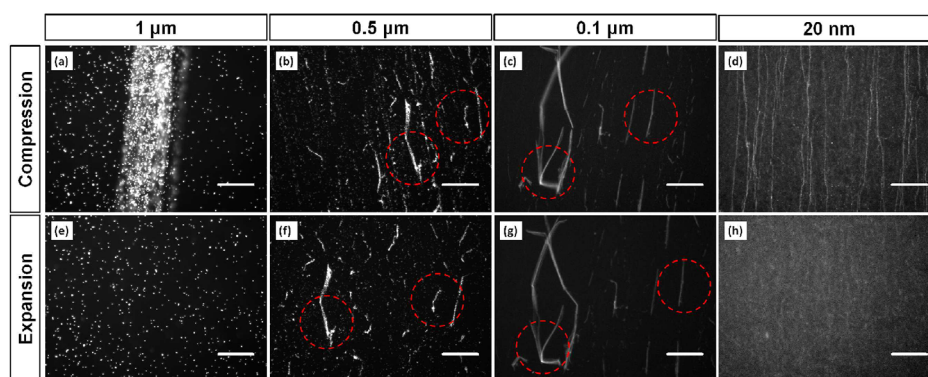


**Figure 2.** Compression and expansion images taken after the fifth cycle for different sizes of particles on the SDS–DODAB monolayer. (a–d) Compression and (e–h) expansion images for the deposition of 1  $\mu\text{m}$ , 0.5  $\mu\text{m}$ , 0.1  $\mu\text{m}$ , and 20 nm particles. The deposition volume is 25  $\mu\text{L}$  for each particle size. The scale bars correspond to 130  $\mu\text{m}$ . The surface pressures for the compression images are (a) 52, (b) 57, (c) 56, and (d) 45 mN/m, respectively. The surface pressure for the expansion images are all close to 0 mN/m. The fluorescent image of particles can be observed directly for 1, 0.5, and 0.1  $\mu\text{m}$  diameters. A small ratio of the  $\text{C}_{12}$  fluorescent probe (1%) is added to the SDS–DODAB stock solution to enhance the image for the 20 nm particle experiment (d and h).

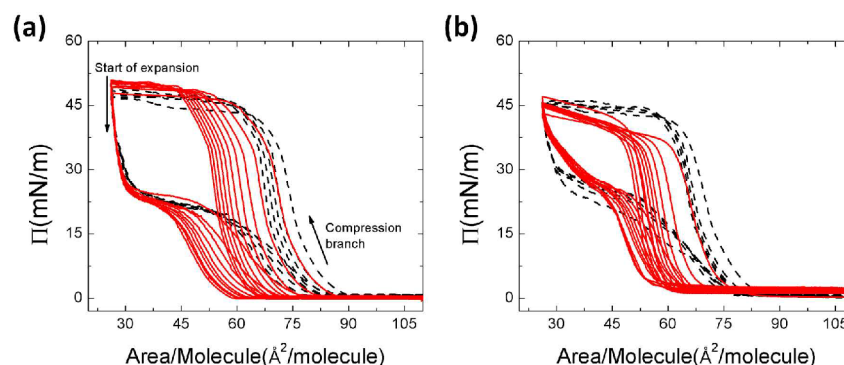


**Figure 3.** Typical surface pressure isotherms for (a) 1  $\mu\text{m}$  and (b) 20 nm (b). The deposition volume is 25  $\mu\text{L}$  for each particle size. All of the isotherms are measured at 295 K. The measurement contains 5 cycles of SDS–DODAB (black dashed line) and 10 more cycles of SDS–DODAB with particles (red line). The isotherms represent reversible folding for the SDS–DODAB monolayer with (a) 1  $\mu\text{m}$  and (b) 20 nm particles, but the surface pressure shows a significant decrease for 20 nm particles.

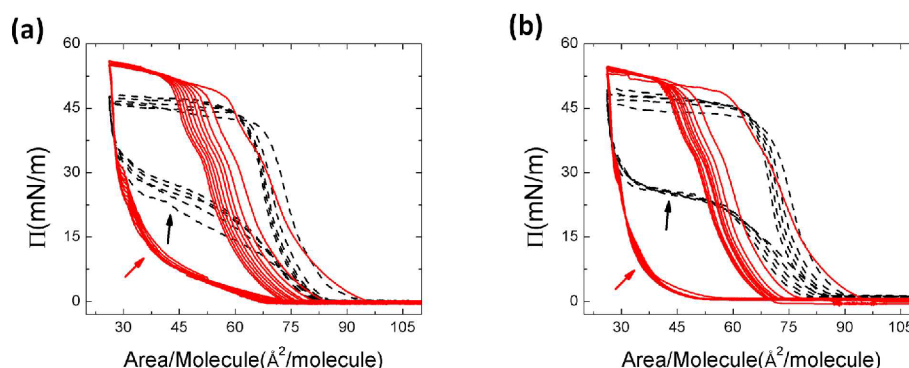


**Figure 4.** Typical surface pressure isotherms for (a) 0.5 and (b) 0.1  $\mu\text{m}$  particles. The deposition volume is 100  $\mu\text{L}$  for each particle diameter. All isotherms are measured at 295 K. The measurement contains 5 cycles of SDS–DODAB (black dashed line) and 10 more cycles of SDS–DODAB with particles (red line). The isotherm represents irreversible folding for the SDS–DODAB monolayer with (a) 0.5 and (b) 0.1  $\mu\text{m}$  particles.

When 0.5 and 0.1  $\mu\text{m}$  particles are distributed in the monolayer, we find a qualitatively different folding process. Figure 2 shows images of compression and expansion for (b, f) 0.5 and (c, g) 0.1  $\mu\text{m}$  particles. As we will demonstrate with isotherm measurements, the structures in the images suggest a transition from reversible to irreversible collapse. In the reversible collapse with 1  $\mu\text{m}$  particles, the orientation of the structures is parallel to the compression barriers. In contrast,

collapsed structures with attached 0.5 and 0.1  $\mu\text{m}$  particles form disordered regions in images resulting from the accumulation of collapsed regions during multiple compression cycles. This is supported by the relative locations of the collapsed regions under compression and expansion. For example, the circles in Figure 2b,c,f,g correspond to the same features in each respective monolayer at different stages in the isotherm cycle.



Surprisingly, with 20 nm particles, as shown in Figure 2d,h, we recover reversible collapse. In this system, the fluorescence is provided by fluorescent tags on C<sub>12</sub> because 20 nm particles do not provide sufficient fluorescence to image collapsed regions. The observed structures match the observations of collapse in pure SDS–DODAB reported in ref 10. In contrast, the structures are smaller than the giant collapse regions observed for 1  $\mu$ m particles. This suggests that the 1  $\mu$ m particles are better at aggregating the collapsed structures than the 20 nm particles.

**Isotherm Measurement.** We used the surface pressure ( $\Pi$ )–area ( $A$ ) isotherm measurement to quantify the reversible and irreversible nature of the collapse. The surface pressure is defined as  $\Pi = \gamma_0 - \gamma$ , where  $\gamma_0$  is the surface tension of pure water and  $\gamma$  is the surface tension of the interface. The surface pressure increases under compression and decreases under expansion. Features of isotherm curves can be attributed to phase changes and the collapse of monolayers.

Isotherm measurements of SDS–DODAB under five compression and expansion cycles are shown in Figures 3 and 4 (black dashed lines). Three different stages are visible under the compression of an SDS–DODAB monolayer. At relatively large surface areas, the monolayer is in a gaslike phase where the surface pressure is effectively zero. The surface pressure starts to rise when the SDS–DODAB monolayer reaches a liquid-expanded (L-E) phase. Finally, the isotherm essentially levels off when the SDS–DODAB monolayer begins to collapse. For SDS–DODAB without particles, this collapse pressure is approximately 45 mN/m. For the case of 0.1  $\mu$ m and larger particles, there is also a small kink in the isotherm at approximately 33 mN/m. This is potentially the onset of a more ordered phase. This is especially true for cases of 0.1 and 0.5  $\mu$ m particles, where the kink is more pronounced.

A key measure of the system behavior is the shift, if any, in the lift-off point. The lift-off point is where the surface pressure begins to rise from zero, which corresponds to the boundary between the gaslike and L-E phases. The corresponding surface area for this point is proportional to the initial number of molecules at the surface. Therefore, a negative shift in the lift-off point corresponds to net material loss from the interface. In the isotherm measurements of SDS–DODAB, the horizontal axis in Figures 3 and 4 is the area per molecule based on the initial number of molecules on the surface. We find shifts in the lift-off point between each compression cycle in the pure SDS–DODAB monolayer. The shift between the first and second compressions is consistently larger than the rest of the shifts in the pure SDS–DODAB monolayer and is in part due to the equilibration of the SDS–DODAB monolayer. Subsequent shifts are due to the observed leakage of monolayer material at the boundaries when high surface pressures are reached. This is observed independently of the collapse mode. Subsequent shifts in the lift-off point occur when particles are added to the system and if additional material is lost due to collapse mechanisms. These features of the isotherm will be discussed in more detail in subsequent sections.

Isotherm measurements after the deposition of particles provide insight into the impact of particle size on the folding of the monolayer. Ten additional isotherm cycles are performed on the monolayer with particles. The resulting curves (red) are shown in Figures 3 and 4 for additions of 25  $\mu$ L of different particle solutions. It is worth noting that all of the isotherm measurements are from the SDS–DODAB monolayer upon the deposition of particles and no additional fluorescent probe.

We use the fluorescent probe only to enhance the imaging of collapse with 20 nm particles during optical measurements. There are two main classes of isotherm results corresponding to reversible and irreversible collapse. Figure 3a,b illustrates isotherm measurements for the reversible collapse of 1  $\mu$ m and 20 nm particles. For 1  $\mu$ m particles, there is no significant change in the isotherm curves and the folding pressure. Of particular note is the behavior under expansion that consists of an initial drop in surface pressure (the stretching of uncollapsed regions) and a plateau region (the unfolding regime).<sup>11</sup> The 20 nm particles exhibit the same reversible expansion behavior; however, there is a significant reduction in the collapse pressure. We observe a decrease from about 45 to 38 mN/m, which is about 15% decrease.

Figure 4 illustrates isotherm measurements with the irreversible collapse of 0.5 and 0.1  $\mu$ m particles. For these systems, the expansion plateau disappears (black and red arrows in Figure 4a,b) from the isotherm. This is consistent with the optical measurements that indicate an aggregation of collapsed structures and a lack of unfolding under expansion.

**Material Loss and Surface Pressure Analysis.** A general feature of isotherm measurements is the horizontal shift of the lift-off point. A direct explanation is that there is a net material loss from the interface during the collapse process. In our system, an addition of particles does not simply shift the lift-off point but significantly changes the shape of the isotherm curve. Therefore, the shift of lift-off point is not sufficient to represent the material loss from the interface with the deposition of particles quantitatively. To quantify the material loss better, we use a model (Volmer's equation) to fit the liquid-expanded portion of the isotherm measurement.<sup>28–30</sup> The model relates the surface pressure to an effective area for the material in the monolayer in the following fashion:

$$\Pi = \frac{kT\omega}{\omega_0} \left( \frac{1}{A - \omega} \right) - \Pi_{\text{coh}} \quad (1)$$

In the equation,  $\Pi$  is the surface pressure,  $\Pi_{\text{coh}}$  is the cohesion pressure,  $k$  is the Boltzmann constant,  $T$  is the temperature,  $\omega_0$  is the molecular area per water molecule,  $A$  is the available surface area per insoluble molecule, and  $\omega$  is the average effective molecular area of an insoluble species. One can write the available surface area per molecule in terms of the actual trough area  $A_T$  and the number of molecules in the system  $n$  as  $A = A_T/n$ . The effective molecular area is an intrinsic property of the system, but we can multiply the expression through by the number of molecules and rewrite it as

$$\Pi = \frac{kT}{\omega_0} \left( \frac{n\omega}{A_T - n\omega} \right) - \Pi_{\text{coh}} \quad (2)$$

This allows us to define the effective total molecular area  $\omega_{\text{eff}} = n\omega$  and fit to the expression

$$\Pi = \frac{kT}{\omega_0} \left( \frac{\omega_{\text{eff}}}{A_T - \omega_{\text{eff}}} \right) - \Pi_{\text{coh}} \quad (3)$$

The advantage of this expression is that the total area  $A_T$  is measured directly and the fit parameter  $\omega_{\text{eff}}$  can be used to characterize the material loss because of changes in  $n$ . A typical fit result for the isotherm data is shown in Figure 5. For the case of the pure monolayer, we measure a slight decrease in  $\omega_{\text{eff}}$  with an increasing number of cycles resulting from the previously discussed leakage of monolayer material through

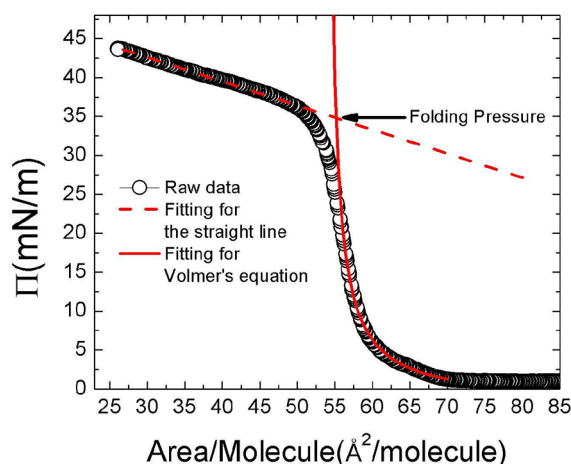


**Figure 5.** Fitting of the isotherm curve. The hollow circles indicate the raw data for our isotherm measurement. The red solid line is the fit to Volmer's equation in the L-E phase. The red dashed line is the fit to the folding state. The crossover point indicates the estimated folding pressure for the folding monolayer.

the barrier. In addition to characterizing the material loss, we fit the isotherm with a straight line in the folding region. The crossover point with the fitting curve of Volmer's equation allows us to define a single folding pressure for the monolayer in the presence of particles (Figure 5).

Figure 6 illustrates how we use both the lift-off point and the fits to eq 3 to quantify the impact of particle addition on the

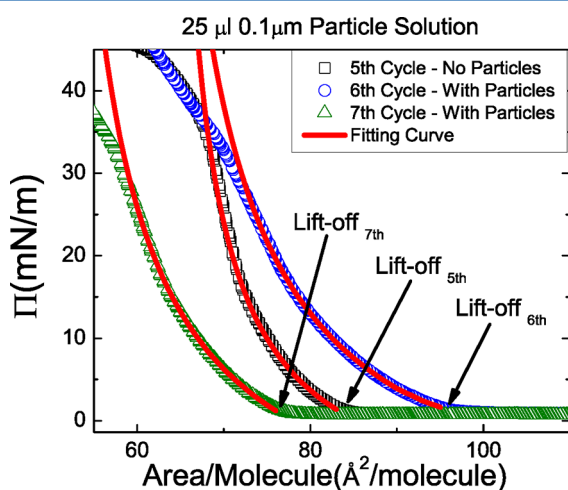


**Figure 6.** Fitting of the isotherm measurement after depositing  $0.1\ \mu\text{m}$  particles. The red lines are fits of the isotherm curve in the L-E phase for the fifth, sixth, and seventh isotherm cycles. A positive shift of the lift point is shown between the fifth and sixth cycles. With further compression, a large amount of the negative shift of the lift-off point between the sixth and seventh cycles can be seen. In this situation, we find a significant amount of material loss at the sixth cycle, which is the first compression of the SDS–DODAB monolayer with the deposition of  $0.1\ \mu\text{m}$  particles.

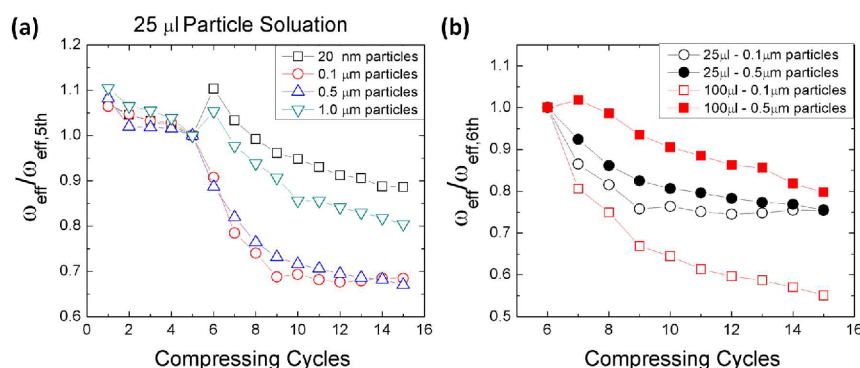
monolayer dynamics. Figure 6 focuses on the portion of the isotherm just before the lift-off point and the initial portion of the L-E phase. We illustrate the case for  $0.1\ \mu\text{m}$  particles using the fifth cycle (last cycle without particles, black open squares), the sixth cycle (first cycle immediately after particle deposition, blue open circles), and the seventh cycle (green open triangles).

The initial deposition of particles will shift the lift-off point to the right by an amount proportional to the effective area of the added material. This is the difference between the fifth and sixth cycle lift-off points in Figure 6. Though shown only for the  $0.1\ \mu\text{m}$  particles, this shift to the right is observed for all sizes of particles. Ideally, the amount of the shift could be used to determine the number of particles added to the system. However, to compute this, it is necessary to know the location of the particles relative to the monolayer in order to compute the effective area of the particles. By changing the focus of the microscope, we are able to determine that the particles are roughly in the plane of the monolayer. However, our resolution in the location of the focal plane is only a few micrometers, so it is not sufficient to compute the precise fraction of particles in the monolayer. If material is lost during a compression–expansion cycle, then the lift-off point shifts to the left. The relatively large shift between sixth and seventh cycle in Figure 6 illustrates the significant material loss during the compression–expansion of the monolayer in the presence of the  $0.1\ \mu\text{m}$  particles.

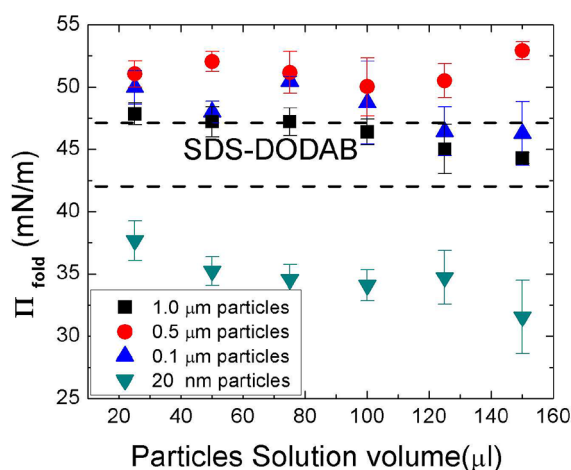
To quantify the loss of material both during and after a compression/expansion cycle better, we used the fit of the L-E phase to eq 3 to determine  $\omega_{\text{eff}}$ . Recall that in our definition of  $\omega_{\text{eff}}$ ,  $\omega_{\text{eff}}$  is proportional to the effective amount of material in the system. Results for  $\omega_{\text{eff}}$  for the first six cycles are presented in Figure 7a. The values of  $\omega_{\text{eff}}$  are normalized to the value in the fifth cycle (the last pure monolayer cycle). There are a number of features of interest. First, there is the slight decrease in  $\omega_{\text{eff}}$  for the first five cycles that was previously discussed and is due to material leakage at barriers. The most important feature is the behavior in the sixth cycle. This is the first compression in the presence of particles. As expected, for the  $1\ \mu\text{m}$  and  $20\ \text{nm}$  particles,  $\omega_{\text{eff}}$  increases for cycle six. This is due to the increase in the effective particle area due to the addition of the particles. This jump is consistent with the shifts in the lift-off points to the right. For subsequent cycles, there is a slow decrease in  $\omega_{\text{eff}}$  due to leakage. In contrast, the deposition of the  $0.1$  and  $0.5\ \mu\text{m}$  particles causes a decrease in  $\omega_{\text{eff}}$  during the sixth cycle. This is in contrast to the shift to the right of the lift-off point and suggests that the particles cause a loss of material during the compression before collapse even occurs. We will discuss this in more detail in the summary. Subsequent cycles show a relatively strong decrease in  $\omega_{\text{eff}}$  that is presumably due to a combination of leakage and particle loss.

Figure 7b compares  $\omega_{\text{eff}}$  versus cycle numbers for 25 and 100  $\mu\text{L}$  of particle solutions for the cases of  $0.1$  and  $0.5\ \mu\text{m}$  particles. (We observe no effect for the reversible case with  $20\ \text{nm}$  and  $1\ \mu\text{m}$  particles.) The behavior is essentially the same for both cases: a strong decrease in  $\omega_{\text{eff}}$  with the initial deposition of particles and a subsequent decrease with additional compression/expansion cycles. However, by normalizing to the value of  $\omega_{\text{eff}}$  in the sixth cycle, one observes that for 25  $\mu\text{L}$  of solution the values of  $\omega_{\text{eff}}$  saturate around the 11th cycle. In contrast, for 100  $\mu\text{L}$  of solution,  $\omega_{\text{eff}}$  decreases monotonically for all cycles. This suggests that the mechanism responsible for the irreversible behavior saturates if the number of particles is sufficiently small. This will be discussed in more detail in the final section.

Finally, Figure 8 shows the effect of particle addition on the collapse pressure for a range of deposition volumes from 25 to 150  $\mu\text{L}$ . As mentioned, the collapse pressure for  $20\ \text{nm}$  particles decreases relative to that for the pure system. A slight increase in collapse pressure occurs for the case of  $0.5$ ,  $0.1$ , and  $1\ \mu\text{m}$



**Figure 7.** (a) Average effective molecular area for the deposition of 25  $\mu$ L of particles of different sizes. The symbols indicate different particle sizes:  $\nabla$ , 1  $\mu$ m;  $\triangle$ , 0.5  $\mu$ m;  $\circ$ , 0.1  $\mu$ m; and  $\square$ , 20 nm. The average effective molecular area is normalized to the fifth cycle to compare the effect of depositing particle solutions. The results show that the deposition of 0.5 and 0.1  $\mu$ m particles leads to a decrease in the average effective molecular area. These two particle sizes correspond to the case of irreversible folding. (b) Average effective molecular area for the deposition of 25 and 100  $\mu$ L of 0.1 and 0.5  $\mu$ m particle solutions. In this case, the average effective molecular area is normalized to the sixth cycle to focus on the effect after the deposition of particles. Continual material loss is shown in the remaining cycles with irreversible folding.



**Figure 8.** Folding pressure vs deposition volume for different particle sizes. The range in between dashed lines is the folding pressure of the SDS-DODAB monolayer. The symbols in the plot indicate  $\blacksquare$ , 1  $\mu$ m particles;  $\bullet$ , 0.5  $\mu$ m particles;  $\blacktriangle$ , 0.1  $\mu$ m particles; and  $\blacktriangledown$ , 20 nm particles. The maximum deposition volume is 150  $\mu$ L. The folding pressure for 1, 0.5, and 0.1  $\mu$ m particles is slightly higher than for the SDS-DODAB monolayer regardless of the deposition volume. However, there is a remarkable decrease in the folding pressure for 20 nm particles, which depends on the deposition volume.

particles, with the smallest effect occurring for the 1  $\mu$ m particles. For volumes from 50 to 100  $\mu$ L, the collapse pressure is independent of the amount of material deposited, and there is only a weak dependence for smaller and larger volumes. The strong shift in collapse pressure for the 20 nm particles suggests that they are the most strongly embedded in the monolayer. This causes the most disruption to the monolayer structure and reduces the pressure required for collapse because the particles provide strong nucleation sites for the collapse. In contrast, the other particles are at best partially embedded or weakly associated with the monolayer headgroups. As such, they do not necessarily nucleate the collapse, though they participate in it.

## DISCUSSION

We have studied the impact of particle deposition on an SDS-DODAB monolayer. There is a critical particle size range that

causes the collapse dynamics to transition from a reversible to an irreversible mode. A monolayer with 1  $\mu$ m and 20 nm particles folds reversibly whereas a monolayer with 0.5 and 0.1  $\mu$ m particles collapses irreversibly. The transition from reversible to irreversible behavior is determined in three ways. First, the direct observation of fluorescent images reveals the aggregation and stability of collapsed domains in the irreversible case. Second, the expansion portions of the isotherms are different in the reversible and irreversible cases. Finally, fits to the compression isotherms provide a direct measure of material loss in the system. Additionally, measurements of the shifts in collapse pressure suggest a stronger embedding of the 20 nm particles in the monolayer. It should also be noted that the independence of any change in collapse pressure from the amount of material added to the system provides indirect evidence that this is really a particle size effect and not a result of the total particle area added to the system.

In the reversible folding state with 1  $\mu$ m particles, the system exhibits reversible giant folding with a slight increase in the folding surface pressure. In this case, because the particle size is much larger than the preferred collapse structure, we propose that the particles remain outside the fold. The monolayer folds reversibly, simply dragging particles with it. The slight increase in the collapse surface pressure is due to the change in the surface tension with particles. With the 20 nm particles, the monolayer exhibits reversible collapse and a significant decrease in the collapse surface pressure. This is reasonable given that the 2D planar structure of the monolayer is most likely disturbed by 20 nm particles, causing a change in the collapse mechanism from giant folds to wrinklelike folds. This results in a dramatic decrease in the folding pressure under compression.

One of the most dramatic features of the measurements is the existence of a finite range of particle sizes that induces material loss. This raises the obvious question: what is the mechanism that selects the relevant particle size? Previously, we showed that there is an energy barrier associated with the folding/unfolding process.<sup>11</sup> This results in the initial elastic stretch of the monolayer under expansion, before unfolding occurs. One possible explanation of the irreversible collapse is the role of additional energy associated with the curvature of the monolayer on the scale of the added particles. For an appropriate particle size, the energy of the collapsed monolayer may be lowered through interaction with the particles. This



idea is consistent with a number of our observations, but at this stage, it remains a conjecture that requires additional theoretical and experimental study.

One indication that the curvature energy plays an important role in the collapse is the relation between vesicle size and the size of the particles causing irreversible collapse. Various methods show that the vesicle size for DODAB and SDS–DODAB mixtures ranges from 100 to 600 nm,<sup>31–36</sup> which is comparable to our critical particle size range. It may be energetically favorable for the monolayer to coat the particles at these high surface pressures. This offers a number of scenarios that could not be distinguished in the current study but will be the subject of future work. One option is that coated particles “pinch off” from the monolayer and form vesicle-like structures in the monolayer. A second option is that the particles covered with SDS–DODAB contact each other and stick together. The accumulation of covered particles and folds could form a jammed state that persists during expansion. We have already observed the aggregation of the particles, but what remains to be determined is whether these aggregates are coated with a monolayer.

The isotherm measurements provide additional indirect evidence that the monolayer has a preference for coating the 0.5 and 0.1  $\mu\text{m}$  particles. Prior to the first compression with particles, the lift-off point in the isotherm exhibits a positive shift after we deposit particles of these sizes. However, even before collapse is induced, the fits of initial compression with these particles is consistent with the loss of material. One explanation of this loss is that the monolayer has a preference for coating particles in this size range. Both the coating of particles with monolayers and the creation of vesicle-like structures can be studied in future work with different fluorescence techniques.

An alternative mechanism to curvature effects is the possible transition to a more ordered phase in the presence of the 0.5 and 0.1  $\mu\text{m}$  particles. For these particles, there is a pronounced kink in the isotherms at around 33 mN/m that corresponds to a reduction in the effective molecular area. This ordering of the monolayer may contribute to the onset of irreversible collapse. Although there is no equivalent kink in the pure monolayer system or the one with 20 nm particles, there is a slight kink with 1  $\mu\text{m}$  particles. Therefore, a more detailed study of the exact ordering induced by the different particles and the impact of this on the collapse is necessary to determine the degree to which this mechanism is relevant. These issues will be the subjects of future studies.

## AUTHOR INFORMATION

### Corresponding Author

\*E-mail: mdennin@uci.edu.

### Notes

The authors declare no competing financial interest.

## ACKNOWLEDGMENTS

We acknowledge the support of NSF-DMR-0907212 and the Research Corporation.

## REFERENCES

- (1) Lu, W.; Knobler, C. M.; Bruinsma, R. F.; Twardos, M.; Dennin, M. Folding Langmuir Monolayers. *Phys. Rev. Lett.* **2002**, *89*, 146107.
- (2) Pocivavsek, L.; Dellsy, R.; Kern, A.; Johnson, S.; Lin, B.; Lee, K. Y.; Cerda, E. Stress and Fold Localization in Thin Elastic Membranes. *Science* **2008**, *320*, 912–916.
- (3) Pocivavsek, L.; Leahy, B.; Holten-Andersen, N.; Lin, B.; Lee, K. Y.; Cerda, E. Geometric Tools for Complex Interfaces: From Lung Surfactant to the Mussel Byssus. *Soft Matter* **2009**, *5*, 1963–1968.
- (4) Leahy, B. D.; Pocivavsek, L.; Meron, M.; Lam, K. L.; Salas, D.; Viccaro, P. J.; Yee, K.; Lin, B. Geometric Stability and Elastic Response of a Supported Nanoparticle Film. *Phys. Rev. Lett.* **2010**, *105*, 058301.
- (5) Pocivavsek, L.; Gavrilov, K.; Cao, K. D.; Chi, E. Y.; Li, D.; Lin, B.; Meron, M.; Majewski, J.; Lee, K. Y. Glycerol-Induced Membrane Stiffening: The Role of Viscous Fluid Adlayers. *Biophys. J.* **2011**, *101*, 118–127.
- (6) Lipp, M. M.; Lee, K. Y. C.; Takamoto, D. Y.; Zasadzinski, J. A.; Waring, A. J. Coexistence of Buckled and Flat Monolayers. *Phys. Rev. Lett.* **1998**, *81*, 1650–1653.
- (7) Takamoto, D. Y.; Lipp, M. M.; von Nahmen, A.; Lee, K. Y.; Waring, A. J.; Zasadzinski, J. A. Interaction of Lung Surfactant Proteins with Anionic Phospholipids. *Biophys. J.* **2001**, *81*, 153–169.
- (8) Ybert, C.; Lu, W.; Möller, G.; Knobler, C. M. Collapse of a Monolayer by Three Mechanisms. *J. Phys. Chem. B* **2002**, *106*, 2004–2008.
- (9) Lee, K. Y. C. Collapse Mechanisms of Langmuir Monolayers. *Annu. Rev. Phys. Chem.* **2008**, *59*, 771–791.
- (10) Coppock, J. D.; Krishan, K.; Dennin, M.; Moore, B. G. Fluorescence Microscopy Imaging of Giant Folding in a Catanionic Monolayer. *Langmuir* **2009**, *25*, 5006–5011.
- (11) Boatwright, T.; Levine, A. J.; Dennin, M. Tracking Giant Folds in a Monolayer. *Langmuir* **2010**, *26*, 12755–12760.
- (12) Olafsen, J., Ed.; *Experimental and Computational Techniques in Soft Condensed Matter Physics*; Cambridge University Press: New York, 2010.
- (13) Bourdieu, L.; Daillant, J.; Chatenay, D.; Braslau, A.; Colson, D. Buckling of Polymerized Monomolecular Films. *Phys. Rev. Lett.* **1994**, *72*, 1502–1505.
- (14) Saint-Jalmes, A.; Graner, F.; Gallet, F.; Houchmandzadeh, B. Buckling of a Bidimensional Solid. *Europhys. Lett.* **1994**, *28*, 565–571.
- (15) Schief, W. R.; Touryan, L.; Hall, S. B.; Vogel, V. Nanoscale Topographic Instabilities of a Phospholipid Monolayer. *J. Phys. Chem. B* **2000**, *104*, 7388–7393.
- (16) Baoukina, S.; Monticelli, L.; Risselada, H. J.; Marrink, S. J.; Tieleman, D. P. The Molecular Mechanism of Lipid Monolayer Collapse. *Proc. Natl. Acad. Sci. U.S.A.* **2008**, *105*, 10803–10808.
- (17) Pocivavsek, L.; Frey, S. L.; Krishan, K.; Gavrilov, K.; Ruchala, P.; Waring, A. J.; Walther, F. J.; Dennin, M.; Witten, T. A.; Lee, K. Y. Lateral Stress Relaxation and Collapse in Lipid Monolayers. *Soft Matter* **2008**, *4*, 2019–2029.
- (18) Notter, R. H.; Tabak, S. A.; Mavis, R. D. Surface Properties of Binary Mixtures of Some Pulmonary Surfactant Components. *J. Lipid. Res.* **1980**, *21*, 10–22.
- (19) Enhorning, G. Pulsating Bubble Technique for Evaluating Pulmonary Surfactant. *J. Appl. Physiol.* **1977**, *43*, 198–203.
- (20) Utell, M. J.; Mariglio, J. A.; Morrow, P. E.; Gibb, F. R.; Speers, D. M. Effects of Inhaled Acid Aerosols on Respiratory Function: The Role of Endogenous Ammonia. *J. Aerosol Med.* **1989**, *2*, 141–147.
- (21) Michaels, R. A.; Kleinman, M. T. Incidence and Apparent Health Significance of Brief Airborne Particle Excursions. *Aerosol Sci. Technol.* **2000**, *32*, 93–105.
- (22) Yang, S. C.; Yang, S. P. Respiratory Function Changes from Inhalation of Polluted Air. *Arch. Environ. Health* **1994**, *49*, 182–187.
- (23) Bakshi, M. S. S.; Zhao, L.; Smith, R.; Possmayer, F.; Petersen, N. O. Metal Nanoparticle Pollutants Interfere with Pulmonary Surfactant Function in Vitro. *Biophys. J.* **2008**, *94*, 855–868.
- (24) Tatur, S.; Badia, A. Influence of Hydrophobic Alkylated Gold Nanoparticles on the Phase Behavior of Monolayers of DPPC and Clinical Lung Surfactant. *Langmuir* **2011**, *28*, 628–639.
- (25) Fan, Q.; Wang, Y. E.; Zhao, X.; Loo, J. S. C.; Zuo, Y. Y. Adverse Biophysical Effects of Hydroxyapatite Nanoparticles on Natural Pulmonary Surfactant. *ACS Nano* **2011**, *5*, 6410–6416.
- (26) Schleh, C.; Muhlfield, C.; Pulskamp, K.; Schmiedl, A.; Nassimi, M.; Lauenstein, H.; Braun, A.; Krug, N.; Erpenbeck, V.; Hohlfield, J.

The Effect of Titanium Dioxide Nanoparticles on Pulmonary Surfactant Function and Ultrastructure. *Respir. Res.* **2009**, *10*, 90.

(27) Gonçalves da Silva, A. M.; Viseu, M. I. Synergism in Mixed Monolayers of Cationic and Anionic Surfactants. *Colloids Surf., A* **1998**, *144*, 191–200.

(28) Fainerman, V. B.; Vollhardt, D. Surface Pressure Isotherm for the Fluid State of Langmuir Monolayers. *J. Phys. Chem. B* **2006**, *110*, 10436–10440.

(29) Miller, R.; Fainerman, V. B.; Kovalchuk, V. I.; Grigoriev, D. O.; Leser, M. E.; Michel, M. Composite Interfacial Layers Containing Micro-Size and Nano-Size Particles. *Adv. Colloid Interface Sci.* **2006**, *128–130*, 17–26.

(30) Fainerman, V.; Lucassen-Reynders, E.; Miller, R. Description of the Adsorption Behaviour of Proteins at Water/Fluid Interfaces in the Framework of a Two-Dimensional Solution Model. *Adv. Colloid Interface Sci.* **2003**, *106*, 237–259.

(31) Vieira, D.; Ribeiro, A. C. Cationic Nanoparticles for Delivery of Amphotericin B: Preparation, Characterization and Activity in Vitro. *J. Nanobiotechnol.* **2008**, *6*, 6.

(32) Cocquyt, J.; Olsson, U.; Olofsson, G.; Van der Meeren, P.; , Temperature Quenched DODAB Dispersions: Fluid and Solid State Coexistence and Complex Formation with Oppositely Charged Surfactant. *Langmuir* **2004**, *20*, 3906–3912.

(33) Barreleiro, P. C. A.; Olofsson, G.; Brown, W.; Edwards, K.; Bonassi, N. M.; Feitosa, E. Interaction of Octaethylene Glycol n-Dodecyl Monoether with Dioctadecyldimethylammonium Bromide and Chloride Vesicles. *Langmuir* **2002**, *18*, 1024–1029.

(34) Pacheco, L. F.; Carmona-Ribeiro, A. M. Effects of Synthetic Lipids on Solubilization and Colloid Stability of Hydrophobic Drugs. *J. Colloid Interface Sci.* **2003**, *258*, 146–154.

(35) Vieira, D. Synthetic Bilayer Fragments for Solubilization of Amphotericin B. *J. Colloid Interface Sci.* **2001**, *244*, 427–431.

(36) Binder, W. H.; Sachsenhofer, R.; Farnik, D.; Blaas, D. Guiding the Location of Nanoparticles into Vesicular Structures: A Morphological Study. *Phys. Chem. Chem. Phys.* **2007**, *9*.